[4]With respect to the line of flight of the V^0, the transverse-momentum distribution of the negative particles from the V^0 peaks at 0.0, 0.1, and 0.2 GeV/c for γ, Λ, and K^0, respectively.

[5]T. M. Knasel, DESY Report Nos. 70/2 and 70/3, 1970 (unpublished). With limited statistics and after making appropriate cuts on the data, the γ-length distribution for this experiment has been found to be consistent with the above cross-section determination.

[6]In the pp center-of-mass frame, s = (total energy)^2, E^* is the photon energy, and P_L^* and $P_\perp$ its longitudinal and transverse momenta. We compute Feynman's x variable from $x = P_L^*/P_{\max}^*$, with $P_{\max}^* = 2.16$ GeV/c.

[7]G. Neuhofer *et al.*, Phys. Lett. 37B, 438 (1971); 38B, 51 (1972).

[8]V. Blobel *et al.*, DESY Report No. 73/36, 1973 (unpublished).

[9]H. J. Lipkin and M. Peshkin, Phys. Rev. Lett. 28, 862 (1972).

[10]J. Hohnerkamp and K. M. Mütter, Nucl. Phys. B38, 565 (1972).

[11]See, for example, V. D. Barger and D. B. Cline, *Phenomenological Theories of High Energy Scattering* (Benjamin, New York, 1969), Chap. 5.

[12]R. N. Cahn and M. B. Einhorn, Phys. Rev. D 4, 3337 (1971).

[13]Particle Data Group, LBL Report No. UCRL-20000 *NN*, 1970 (unpublished). From the published values, the weighted average is estimated as σ_T(inelastic) = (29.1 ± 2.3) mb.

[14]The implications of such correlations have been discussed by E. L. Berger, D. Horn, and G. H. Thomas [Phys. Rev. D 7, 1412 (1973)].

[15]Inelastic topological cross sections were extrapolated from the 12.88-GeV/c data of B. Y. Oh and G. Smith (private communication).

[16]H. Bøggild *et al.*, Nucl. Phys. B27, 285 (1971). The γ conversions in this experiment were counted but not measured. We have computed the values of $\langle n_{\pi^0} \rangle$ shown in Fig. 4 from the raw data in this publication. The errors are statistical only.

[17]G. Charlton *et al.*, Phys. Rev. Lett. 29, 1759 (1972). The data shown are the most recent results. See K. Jaeger *et al.*, paper submitted to Berkeley Conference, August, 1973 (unpublished).

[18]F. T. Dao *et al.*, Phys. Rev. Lett. 30, 1151 (1973).

[19]G. Flügge *et al.*, in *Proceedings of the XVI International Conference on High Energy Physics, Chicago-Batavia, Ill., 1972,* edited by J. D. Jackson and A. Roberts (NAL, Batavia, Ill., 1973), Vol. 1, p. 561.

PHYSICAL REVIEW D VOLUME 8, NUMBER 11 1 DECEMBER 1973

Proton Compton Scattering at 0.55-to-4.5-GeV Energy and 0.12-to-1.0-(GeV/c)^2 Momentum Transfer*

M. Deutsch, K. J. Cleetus,† L. Golub,‡ D. F. Jacobs,§
P. Kijewski, E. Loh,‖ G. Marini,** P. M. Patel,††
D. Potter,‡‡ R. Stiening,§§ and K. Tsipis‖‖

Laboratory of Nuclear Science and Department of Physics, Massachusetts Institute of Technology, Cambridge, Massachusetts 02139

(Received 4 April 1973)

Results are presented on the elastic scattering of photons by protons. The incident photon energy ranged from 0.55 GeV to 4.5 GeV, and the four-momentum transfer t ranged from 0.12 to 1.0 (GeV/c)^2. The data at large angles, $60° < \theta^* < 115°$, are characterized by a pronounced excitation of the $D_{13}(1518)$ resonance, a shoulder in the 1688-MeV mass region, and a precipitous drop thereafter in the cross section as a function of incident energy. The low-t data are characterized by a diffraction slope of 5 (GeV/c)$^{-2}$. The data are inconsistent with the predictions of the vector-dominance model if the latter is restricted to ρ^0, ω, and ϕ vector mesons.

I. INTRODUCTION

We report a series of experiments on the elastic scattering of photons by protons conducted at the Cornell and Cambridge Electron Accelerators. The incident photon energy ranged from 0.55 to 4.5 GeV and the four-momentum transfer from 0.12 to 1.0 (GeV/c)^2. The experiments fall into two groups:

(i) "Large-angle" experiments with incident photon energy < 2.5 GeV and the center-of-mass angles in the range $60° < \theta^* < 115°$. The main motivation here was to search for resonance structure in the differential cross section.

The data exhibit a decrease of two orders of magnitude in the cross section in going from 0.5 to 2.5 GeV in the incident momentum. We were therefore limited by counting rate in extending these large-angle experiments to higher energies. A similar precipitous drop in cross section is

observed in hadron-hadron collisions.

(ii) "Small-angle" experiments with incident photon energy up to 4.5 GeV and small center-of-mass scattering angles in the range $15° < 0^* < 35°$, the four-momentum transfer interval being $0.14 < -t < 0.41$ $(\mathrm{GeV}/c)^2$. The main motivation here was to study the diffraction slope of the differential cross section, and to compare the forward extrapolated cross section with the optical-theorem limit provided by the total photon-hadron absorption measurements. Again, we find that the Compton process exhibits a behavior similar to that observed in hadron-hadron collision.

Each group of measurements consisted of several data runs. Table I summarizes the entire series of measurements.

The overlap between the series was made deliberately to check for internal consistency in absolute normalization of the data.

The data for run $A1$ have already been published[9] and are included here for completeness.

The elastic scattering of electrons and photons on protons has played a unique role in elucidating the structure of the proton. The former measures the charge and the magnetic moment distribution whereas the latter—referred to as the proton Compton effect hereafter—measures the electric and magnetic polarizabilities of the proton. The development of dispersion techniques in strong-interaction physics put these notions on a quantitative footing—the first application of these techniques was to the proton Compton effect.[1] A review of the theoretical and experimental situation of the proton Compton effect below 400 MeV, with a fairly complete list of references, is given in Ref. 2. In the neighborhood of the $D_{13}(1518)$ and below, the isobar model provides an adequate description.[3] At higher incident photon energies, the number of parameters inherent in such a model and the difficulty of taking into account multipion exchange contributions make this model quite unwieldy. The vector-dominance model[4,5] (VDM) provides an alternative framework for phenomenologically relating the Compton effect to photoproduction of ρ^0, ω, and ϕ mesons—for incident photon energies high enough that the effects of the vector-meson masses are not important. In the absence of a fundamental theory exhibiting the dependence of the matrix elements on the masses of these mesons, the lower-energy limit at which this model ceases to be valid cannot be specified. Moreover, a precise confrontation with the vector-dominance model is difficult because of the following fact: The major contribution to the VDM prediction comes from the ρ^0 photoproduction cross section which has to be extracted from the experimentally determined dipion photoproduction cross section. The ρ^0 resonance has a large width and its excitation function does not show a simple Breit-Wigner form—so that the ρ^0 production is accompanied by a sizeable coherent dipion continuum production in the same mass region.[5,6] Hence the extracted magnitude of ρ^0 photoproduction is strongly model-dependent. Nonetheless, the discrepancies reported here are sufficiently large to suggest that VDM in its present form is not valid. The bearing of additional vector mesons, like ρ', on this discrepancy will be discussed in Sec. V.

Preliminary reports[8] on part of the data given here have been presented earlier. Published data appear in Refs. 9 to 14 and will be referred to in the discussion of our results.

In Sec. II we discuss first the rationale of the experimental strategies employed, and then the kinematic relations and phase-space diagrams. Section III gives details of the apparatus while Sec. IV discusses the data reduction. Section V gives the results and conclusions.

II. DESIGN OF EXPERIMENTS

The principal experimental problem in these measurements is the separation of the elastic scattering process

$$\gamma + p \rightarrow \gamma + p \tag{1}$$

from the much more probable single pion production

$$\gamma + p \rightarrow \pi^0 + p, \quad \pi^0 \rightarrow \gamma + \gamma \tag{2}$$

and, to a lesser extent, from other, inelastic processes.

We identified the recoil particle as a proton by measuring dE/dx and range, or bending in a magnetic field, dE/dx and time of flight. In order to establish the electromagnetic nature of the scattered particle, we measured the total Čerenkov light produced in lead glass blocks. Its neutral character was ascertained by observing the origin of the ionizing shower produced in a multiplate optical spark chamber. During some of the experiments we also used a veto counter in front of the shower detector. With the target proton at rest and with the nature of the secondary particles identified, process (1) can be completely reconstructed from six independent combinations of the nine momentum components, e.g., the directions only of $\vec{k}$, $\vec{k}'$, and $\vec{p}$, the momenta of the incident and scattered photons and the recoil proton, respectively; or the magnitude and direction of $\vec{k}$ and $\vec{k}'$. However, the differential cross sections for process (2) are typically 30 times as large as those for process (1) in the kinematic regions

covered. The kinematics of the decay favors emission of one γ ray nearly satisfying the conditions for process (1). Therefore, the background accidentally satisfying the one-constraint fit is quite large with the achievable resolution and at least one additional constraint is required. We have chosen to measure the angles of both secondary particles and the energy of the recoil proton. The direction of the incident photon was, of course, known. With this additional constraint the background due to single π^0 production is tolerable, although it still contributes significantly to the final error. In addition, a rough (±20%) measurement of the energy k' serves to suppress other background processes.

The choice of track detection technique was determined by the following considerations. The differential cross sections measured are as low as 10^{-32} cm^2/sr. The detector must therefore subtend a reasonably large solid angle. Discrimination against inelastic processes requires good spatial and time resolution. Finally, the detector must support the background of electrons and photons encountered with bremsstrahlung beams. By far the most economical technique satisfying these requirements is the use of spark chambers. When these experiments were planned, the only practical recording method for spark chambers was photography.

The proton angle was measured by two thin-foil optical spark chambers facing the hydrogen target. The angle of $\vec{k}'$ was found from the shower origin in a chamber with lead or tantalum plates (SC) and from the reaction vertex reconstructed by the intersection of the incident beam with the recoil track.

The recoil proton energy varied between about 70 and 370 MeV (Fig. 1). We used an optical spark chamber with 30 aluminum plates of graded thickness to measure the proton range for the lower energies and a simple deflecting magnet for the experiments with larger momentum transfer. The energy of the scattered γ ray, $\vec{k}'$, was determined from the pulse height in a total absorption Čerenkov counter ($\check{C}$). An attempt was made to account for the shower energy lost in the two radiation lengths of the spark chamber SC. Corrections based on the starting point of the shower and on spark count yielded only marginal improvement of the resolution and were abandoned.

Because of the wide range of c.m. momentum and angle covered in these experiments, the parameters determining the acceptance of the apparatus varied considerably among the runs. One design aim was to limit the aperture in one arm (proton or photon) for all accepted events and to make the aperture of the other arm sufficiently

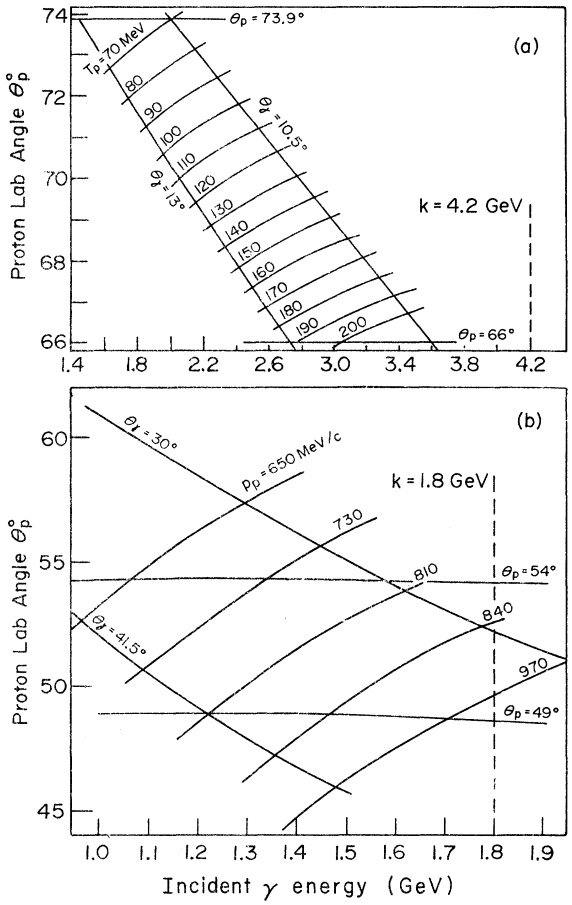

FIG. 1. Typical phase-space acceptance of the apparatus. (a) Small-angle measurements utilizing the range technique; (b) large-angle measurements utilizing the magnetic spectrometer.

large to allow reliable extrapolation of the background to the Compton kinematic peak.

When the range chamber was used, the azimuthal (vertical) aperture was limited by a lead collimator in front of the shower detector, except in runs $D2$ to $D7$ (see Table I). When the magnetic spectrometer was used the azimuthal aperture was defined in the chambers $T1$ and $T2$ so that no particles could strike physical obstructions.

The acceptance limits in the reaction plane are more complicated. Figure 1(a) illustrates the situation in one typical small-angle run, using the range chamber. For protons with kinetic energy in the range $80 < T < 170$ MeV [i.e., $0.15 < t < 0.32$ (GeV/c)^2] the acceptance for events at all target points is entirely determined by the physical aperture of the shower detector. The range of angles accepted in the proton arm depends on the position of the reaction vertex in the hydrogen target. For example, for $T = 200$ MeV only about 50% of the target is effective. Some data from this re-

TABLE I. List of experiments with kinematic details and nonmenclature used in describing them. Column 6 refers to Cornell Electron Synchrotron and the Cambridge Electron Accelerator.

Time (hours)	Runs	k	θ_c^*	Recoil energy measurement	Data series
~80	$A1$–$A3$	0.55 to 0.9	65°–115°	Range technique	Cornell (1962–1963)
~30	B	0.8 to 1.3	~65°	Range technique	CEA (1964–1965)
~240	$C1$–$C3$	0.7 to 2.7	~65°	Magnetic spectrometer	CEA (1966–1967)
~160	$D1$–$D7$	1.3 to 4.5	15°–30°	Range technique	CEA (1968–1969)

gion are included in our results and the probable error of these points is increased by the uncertainty in target volume and background subtraction. Figure 1(b) illustrates a typical large angle run, using the magnetic spectrometer. Here the situation is reversed: For incident γ-ray energies $1250 < k < 1560$ MeV the acceptance is mainly determined by the geometric aperture of the spectrometer. (The angular position of this aperture varies slightly with proton energy because it is limited after the magnetic deflection.) For $1080 < k < 1250$ MeV and $1560 < k < 1680$ MeV the boundaries of the shower detector eliminate events from part of the target. For the highest and lowest of these energies about 70% of the target is effective. Again, some data in these regions are included in our results.

Beyond these energies, the boundaries of the magnet pole pieces impose limits on the acceptance and this is indicated in Fig. 1(b) by nominal limiting momenta.

Approximately 10^6 photographs were processed in the course of the measurements reported here. About one-third of these required complete measurement of track and shower coordinates and geometric reconstruction. The effort of manually encoding this number of events seemed excessive for the results expected. Therefore we designed and assembled a fully automatic film scanning and measuring system, SPASS, using the display CRT of a PDP-1 computer as a program-controlled flying-spot scanner.[15] The film transport was a TRAID camera of the same type used to obtain the photographs. As far as we know this was the first operational, fully automatic scanning and measuring system for spark-chamber photographs. We designed computer programs for longitudinal and stereo track linking, for shower recognition, and for the encoding of digital information recorded on the film. Although developed specifically for the experiments reported in this paper, the SPASS system was used successfully for several other experimental programs.

We monitored the operation of the system on a slave CRT in order to detect scanning and measuring failures and, whenever possible, eliminated them by program modifications. Statistical corrections for the remaining failures were determined primarily by inspecting the original photographs for events in which the computer indicated difficulties, e.g., inconsistencies between the two views. This was found to be more efficient than the more usual procedure of comparing a large, unselected sample of automatically processed data with results of independent hand scanning. The rate of processing events through SPASS was about one-half of the rate of data acquisition. Allowing for film-processing time, it was possible to monitor the results of an ongoing experiment with a delay of about 36 hours.

The signals from the several scintillation and Čerenkov counters provided information used to identify valid events (refer to Sec. IV B). This information was digitally encoded on the film by means of "data lights." During series D these data were also registered on magnetic tape, later merged with the tapes produced by SPASS. Histograms of selected pulse-height and time distributions were monitored during data acquisition to verify proper operation of the apparatus.

Trigger conditions were chosen as loose as consistent with an acceptable rate of film use (about 0.6 events per second) with the beam intensity as high as possible consistent with a tolerable chamber background and accidental coincidence rates. For example, coincidence resolving times in the trigger circuits were substantially longer than the time resolution of the detectors. The effective timing cut was applied to the recorded output of time-to-amplitude converters which also yielded an estimate of accidental coincidences from the wings of the timing curves.

III. APPARATUS

Figure 2 shows a plan view of the apparatus used. In series A, B, and D, the magnetic spectrometer was replaced by a range chamber. In the following sections, we discuss the various parts of the apparatus in detail.

A. Beam and Quantameter

The beam configuration shown in Fig. 3 was employed in series *D* and is typical of the beams used in all the runs.

The internal target was a short straight piece of tungsten ribbon, 0.38 mm thick, 3.0 mm wide. The collimator, 20.3 m downstream from the target, was a block of Hevimet, 10 cm thick, with a hole 9.6 mm in diameter through its center. Downstream from the collimator was an electromagnet used to sweep the beam clear of charged particles. The beam next passed through the accelerator shielding wall and a series of three scrapers, placed so as to minimize the beam halo seen by the detectors. Any part of the beam scattering off the collimator or any part of the halo scattering off a scraper saw only one subsequent surface off which it could scatter back into the beam. At the hydrogen target, about 15 m from the collimator, the beam was an ellipse 1.5 cm wide and 1.6 cm high. After passing through the target, the beam traveled about 8.2 m to enter the quantameter hut. The Wilson quantameters used a 90% helium, 10% nitrogen mixture in most cases. In some of the runs, 95% argon, 5% CO_2 mixture was employed. In all cases, the quantameters were calibrated in an electron beam, by the laboratory staff, with respect to a Faraday cup. During the runs the gas pressure and temperature were periodically checked.

Experiment *B* was the first in the series performed at the Cambridge Electron Accelerator (CEA). It has been necessary to renormalize the

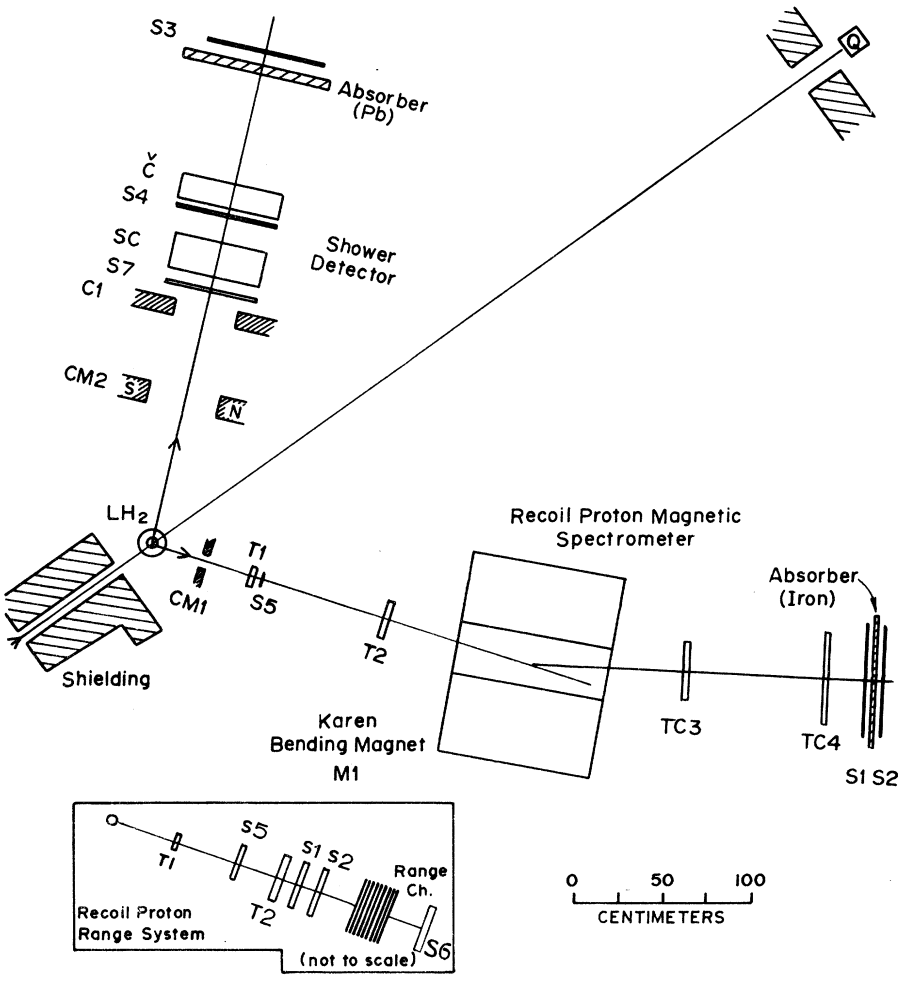

FIG. 2. Plan view of the apparatus. LH_2: Liquid-hydrogen target; *CM*1, *CM*2: Alnico magnets for sweeping soft electrons; *T*1–*T*4: Thin-electrode spark chambers; *S*1–*S*7: Scintillation counters; *SC*: Photon shower spark chamber; *C*: Lead glass counter; *M*1: Spectrometer bending magnet; *Q*: Wilson quantameter. Insert shows proton arm configuration when the energy of the proton was measured using a range chamber.

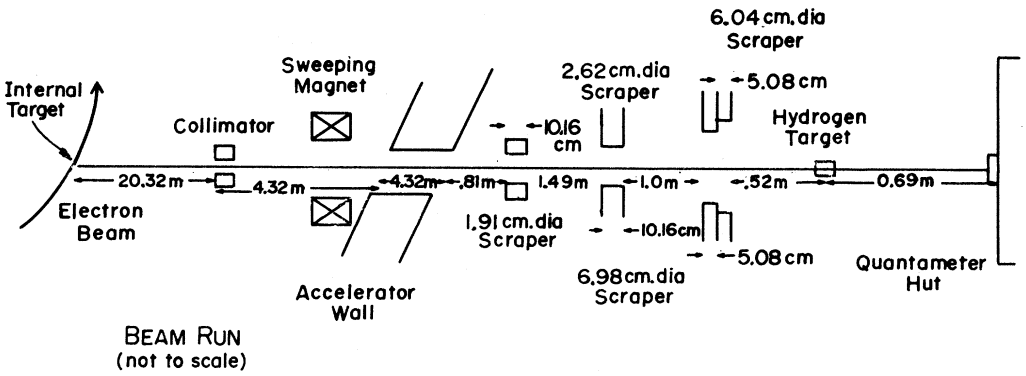

FIG. 3. Beam configuration for experimental runs in series D.

data by a factor 1.4 in order to bring the set of data in line with all others. This is traced to quantameter malfunction in the early stages of CEA operation and there exists evidence from other independent experiments—using the same beam line at that time—to substantiate this correction.

B. Hydrogen Target

The typical target used was a cylinder 5.1 cm in diameter and 5.1 cm in length when empty. The end caps bellied out an additional 3.2 mm at each end when the target was full. The cylinder walls were of 0.19-mm aluminized Mylar; the end caps were of 0.13-mm aluminized Mylar and overlapped the cylinder walls by 7.9 mm at each end. The axis of the cylinder lay on the beam line in series D; in all other runs it was at right angles to the beam line. The pressure was essentially atmospheric, giving a density of 0.07 g/cm^3.

The evacuated scattering chamber which contained the target was a cylinder whose vertical axis approximately coincided with the target center. The walls were of 0.25-mm Mylar, stretched between two 17.8-cm hoops held apart by 1.11-cm-diameter hollow upright rods which were located by holes in the 22.8-cm-diameter aluminum base plate. The rods were positioned so as to clear the incident beam, the recoiling protons, and the scattered photons.

C. The Proton Arm

The proton arm consisted of two thin "tracking" chambers to determine the initial trajectory of the recoil proton, followed by the energy measuring device—range chamber or deflecting magnet—and scintillation counters to provide a trigger signal and to measure dE/dx and time of flight.

Table II lists the characteristics of the counters and chambers used in the several runs. The main trigger and identification function was performed by the counters $S1$ and $S1$, placed either in front of the range chamber or behind the deflecting magnet. A coincidence $S1 \times S2$ was always part of the trigger requirement. The pulse height in these counters was required to correspond to dE/dx deduced from the measured proton energy in the data analysis. In series C and D, the thin counter $S5$ was added to reduce the accidental trigger rate due to stray particles in $S1$ and $S2$. $S5$ and $S2$ provided the signals for proton velocity measurement. The veto counter $S6$, used only in series D, reduced the trigger rate due to particles with excessive range—mostly pions and electrons.

A small permanent magnet $CM1$ with bending power $\approx$2500 gauss-cm located between the hydrogen target and the first tracking chamber proved very valuable in removing soft Compton electrons from the chambers.

The dipole bending magnet "Karen" had a useful aperture of 30 cm$\times$10 cm. The length of the pole piece was 91 cm. The magnet field was measured in two planes; the field plots were then used to compute an aperture over which, by the use of an effective-length approach, the computed particle momentum differed at most by 1% from the value one would obtain by tracing the particle trajectory through the field. We found that this approach simplified our data reduction enormously and the accuracy matched quite well the other sources of errors in obtaining the particle momentum.

Two perpendicular views of all chambers were photographed through plastic field lenses by a single 35-mm camera (TRAID). The images of the several chambers were collected by a system of proton arm. A number of fiducial lights was mounted near the chambers in both views and their position in the laboratory surveyed precisely. Linear interpolation between their positions as measured by SPASS was sufficient to correct distortions

TABLE II. Details of scintillation counters and spark chambers used in the experiment.

Scintillation counters

Runs	$S1$	$S2$	$S3$	$S4$	$S5$	$S6$	$S7$	Trigger logic
$A1$–$A3$	$\frac{1}{2}\times5\times7$ in.	$\frac{1}{2}\times5\times7$ in.	$\frac{1}{2}\times5\times7$ in.	···	···	···	···	$S1\times S2\times\check{C}$
$B1$	$\frac{1}{2}\times5\times7$ in.	$\frac{1}{2}\times5\times7$ in.	$\frac{1}{2}\times5\times7$ in.	···	···	···	···	$S1\times S2\times C$
$C1$–$C3$	$1\times12\times27$ in.	$1\times12\times27$ in.	$1\times12\times27$ in.	$\frac{1}{2}\times13\times24$ in.	$\frac{1}{16}\times3\times4\frac{1}{2}$ in.	···	···	$S1\times S2\times S5\times S4\times\check{C}$
$D1$	$\frac{1}{2}\times7\times11$ in.	$\frac{1}{2}\times7\times11$ in.	$\frac{1}{2}\times11\times12$ in.	$\frac{1}{2}\times11\times12$ in.	$\frac{1}{16}\times3\frac{1}{2}\times5$ in.	$\frac{1}{2}\times11\times12$ in.	$\frac{1}{2}\times5\times10$ in.	$S1\times S2\times S5\times S4\times S7\times\check{C}$
$D2$–$D7$	$\frac{1}{2}\times3\frac{9}{16}\times10$ in.	$\frac{1}{2}\times7\times11$ in.	$\frac{1}{2}\times11\times12$ in.	$\frac{1}{2}\times11\times12$ in.	$\frac{1}{16}\times3\frac{1}{4}\times7\frac{1}{8}$ in.	$\frac{1}{2}\times11\times12$ in.	$\frac{1}{2}\times7\times11$ in.	

Tracking chambers

Experiment	$T1$		$T2$		$T3$		$T4$	
	Dim.	Electrodes [a]	Dim.	Electrodes [a]	Dim.	Electrodes [a]	Dim.	Electrodes [a]
A	$3\frac{1}{2}\times3$ in.	7×0.001 in.	9×6 in.	7×0.001 in.				
B	$5\frac{1}{2}\times3$ in.	9×0.001 in.	9×6 in.	9×0.001 in.				
C	$5\frac{1}{2}\times3$ in.	9×0.001 in.	9×6 in.	9×0.001 in.	$14\times7\frac{1}{4}$ in.	9×0.002 in.	22×9 in.	9×0.0085 in.
D	$6\frac{1}{2}\times4\frac{1}{2}$ in.	5×0.0005 in.	10×7 in.	7×0.001 in.				

Range chamber

Experiment	$A1$, B		$A2$, $A3$, $D1$–$D7$	
	Gap	Thickness of plates [b]	Gap No.	Thickness of plates [b]
	0–11	1.35		0.214
	12–19	2.43	1–3	0.436
	20–28	3.78	4–8	0.623
			9–18	0.882
			19–29	1.361
			30	3.429

[a] All electrodes made of Al foil.
[b] Thickness in g/cm^2 of Al.

in the photographic and measuring optics and in the CRT used for SPASS. The precise position of the chambers themselves was not critical.

D. Shower Arm

The principal components of the shower arm are the total absorption Čerenkov counter C and the shower chamber SC. Counter C consists of an array of 15-cm cubes of lead glass (Schott SF6) each viewed by a photomultiplier (RCA 7046). Six blocks were used in series A and B, eight blocks in series C and D. SF6 glass consists of approximately 70% PbO_2, 30% SiO_2. The 15-cm block represents approximately seven radiation lengths. Light absorption in this glass is quite severe. This, together with fluctuations of the energy loss in the shower chamber (approximately 2 radiation lengths) limits the energy resolution, especially for low-energy showers. The pulse from each photomultiplier was split: One half was integrated and stored on a capacitor for pulse-height encoding; the other half was routed to a linear adder to form a total shower pulse. This was again split: One half, passing through a discriminator, was used for the trigger logic; the other half was integrated and encoded as total shower pulse height.

In the small-angle experiment, series D, two scintillation counters $S4$ and $S7$ were added to the trigger logic, to form a shower signal $C\times S4\times\overline{S7}$. $S4$, located between the chamber and counter C, restricted triggers to photons forming showers in the chamber. $S7$ vetoed charged particles coming from the target or shielding. Granted that the information from these counters becomes redundant once the shower-chamber photograph is available for analysis, these counters served to reduce the background trigger rate at the cost of small connections for absorption and dead time. The inclusion of $S4$ also permitted the use of a shorter coincidence-resolving time. The scintillation counter $S3$ (Fig. 2) was not part of the trigger logic but was used for test and calibration of counter C.

The shower chamber contained 19 aluminum-clad lead (or tantalum) electrodes of about 0.1 radiation length each and six thin aluminum electrodes located to form "guard gaps" in front and back of the chamber. The front guard gaps served to eliminate charged particles. The rear guard gaps helped identify showers produced in the last heavy plates.

Two perpendicular views of the shower chamber were photographed in the same manner as the chambers in the proton arm.

A permanent magnet $CM2$, with bending power ≈9100 gauss-cm helped eliminate charged particles originating at the target.

E. Electronics

The electronic circuits providing the trigger signal were located close to the detection equipment in order to minimize the delay of the high-voltage pulse on the spark chambers. Since the experimental area was not accessible during operation, the diagnostic and digitizing circuits were located in the counting room, 30 m distant. The trigger logic in the configuration of series D is illustrated in Fig. 4. Analog signals from the counters and logic signals from all discriminators and coincidence units were carried to the counting room. The counting-room logic is illustrated in Fig. 5. Digitization of all pulse height and time signals was carried out by a samplehold system PANSY. The analog pulses were stored on capacitors and presented successively to the analog-digital converter of a RIDL 400-channel pulse-height analyzer. The eight-bit digital output was stored in a 96-bit shift register, displayed on data lights, and photographed with the spark chambers. During series D, the bits were also recorded on magnetic tape, later merged with the SPASS output tape. The pulse-height analyzer could be programmed to sort simultaneously information from any four of the sixteen available channels. All pulse-height distributions were thus monitored in rotation.

The over-all dead time, set by digitization, illumination of data and fiducial lights, and by film transport, was about 0.3 sec. During this time the electron beam of the synchrotron was deflected away from the radiation target by a "busy" signal so that no photon beam entered the experimental area. There remained a small (≈1%) correction for multiple events occurring during the same machine cycle.

All relevant counting rates were recorded on scaling circuits. Remote switching of trigger logic circuits allowed periodic testing of circuit operation. Spark-chamber operation was monitored on closed-circuit television.

IV. DATA REDUCTION

A. Track and Shower Reconstruction

The photographs of the proton and shower arms were processed separately by SPASS. Since 90° stereo photography was used, we followed the strategy of reconstructing the entire proton trajectory separately in each view and using comparisons between the two views only to resolve multiple track ambiguities. Reconstruction started with the chamber (other than the range chamber) farthest from the hydrogen target since it rarely contained background tracks. For every track

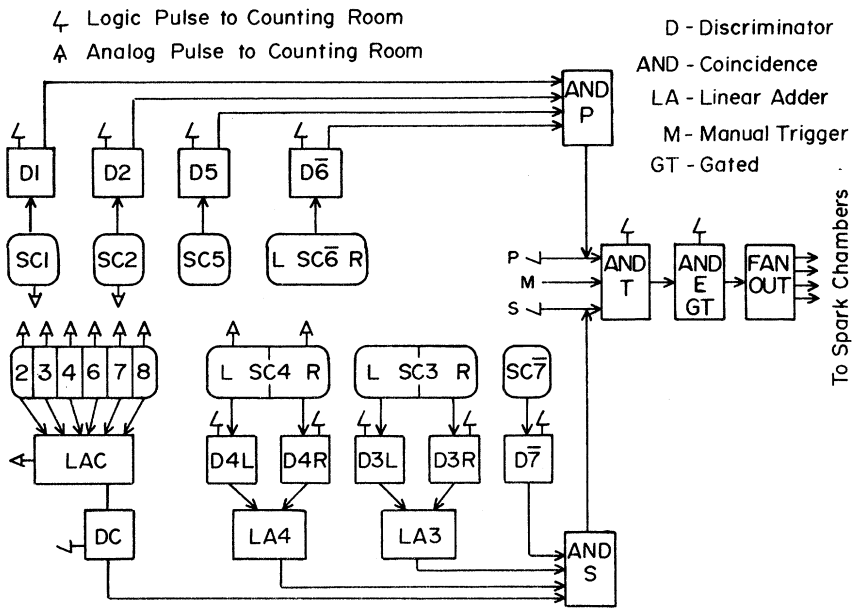

FIG. 4. Block diagram for trigger logic, located on the experimental floor.

with an acceptable angle the intersection with the next chamber was calculated and the region in the vicinity of this coordinate was searched for acceptable tracks. If a track was found it was presumed to be part of the same trajectory, and a new prediction was made for the next chamber, using the coordinates already measured. Prediction across the bending magnet was made with the assumption of straight line segments intersecting in the midplane of the magnet. Appropriate limits were im-

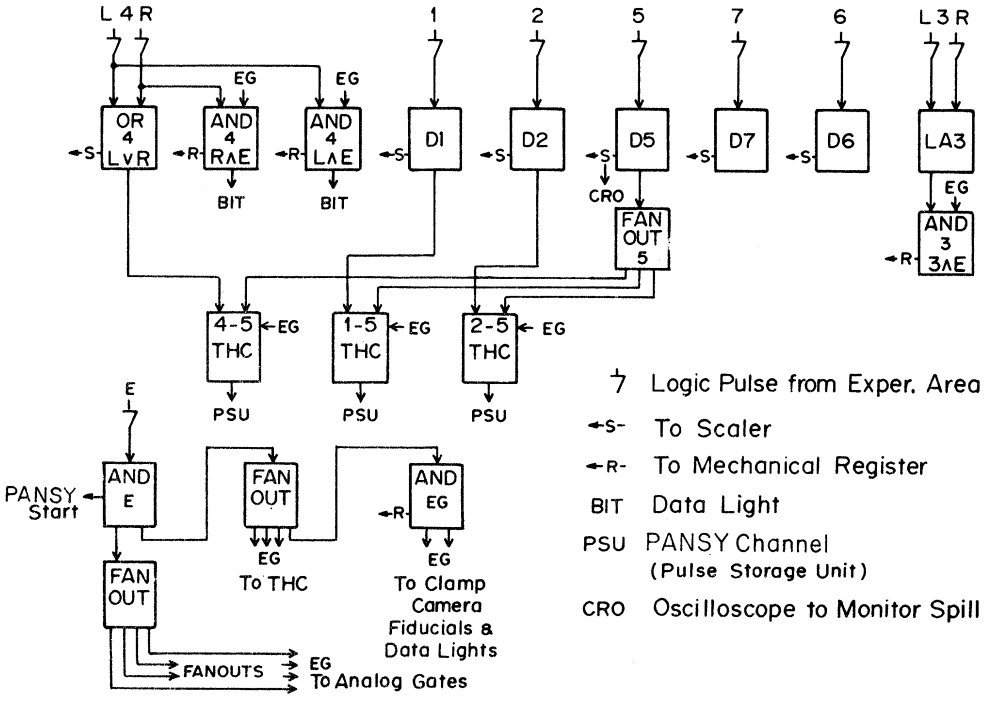

FIG. 5. Block diagram for electronic logic in the counting room.

posed on the acceptable deviations in position and angle of the several tracks linked in a reconstructed trajectory. An acceptable proton trajectory required a properly linked track in every chamber. If more than one acceptable trajectory was reconstructed in both views, the event was rejected as ambiguous. If one view contained a single trajectory but the other view contained more than one, stereo identification was attempted, primarily by matching missing gaps. Any difficulty encountered was encoded with the coordinates for later statistical evaluation. The number of doubtful events never exceeded 5% and visual inspection of a sample showed that the program resolved most cases correctly. In the range chamber tracks were not followed past large-angle scattering points and the range found in the two views was required to agree within one gap. This procedure is consistent with the correction for nuclear collision loss applied to the cross-section results.

Shower reconstruction was more complex and evolved as the experiments progressed. Here also, the two views were treated separately unless ambiguities arose. The first gap following the guard gaps were searched for sparks. For each spark found, a zone in the next few gaps was examined for a track. If at least three consecutive sparks were found, subsequent gaps were scanned in expanding zones designed to include the main cone of the developing shower. A record was kept of the total number of sparks encountered and of any empty gaps. A valid shower required a minimum number of sparks, depending on the number of plates in which the shower developed. In addition the shower had to contain some sparks in the rear guard gaps. If no acceptable shower originated in the first gap, further gaps were searched for shower origins. Sparks previously linked in an abortive shower reconstruction were not accepted as shower origins but could be included in the later shower development. The search was continued through 16 gaps, if necessary, until a valid shower was found. When a shower was found to originate in the first or second lead plate, the guard gaps were examined to determine whether it originated from a charged particle. Soft electrons in the guard gaps sometimes occurred accidentally near the start of a shower and appropriate algorithms were designed to minimize the loss of real photon showers due to this effect.

We have developed fairly elaborate routines for the reconstruction of events with multiple showers in another experiment.[16] It was found that these contributed little to the recovery of valid events in the present experiment.

Substantially, the entire reconstruction of the proton trajectories and showers was carried out by SPASS interacting with the photographic image. The output tape contained only the coordinates and angles of the accepted tracks and showers, the shower size, codes identifying any special problems such as multiple tracks, and the digital information encoded on the film.

B. Event Reconstruction and Selection

The results of the track and shower reconstruction were processed further, using the PDP-1 Computer, with a program SORT which performed the transformation to laboratory coordinates, the kinematic calculations, and the multidimensional event sorting. The general strategy of event reconstruction first rejected spurious events in each arm separately. For example, protons were rejected if the energy loss in the scintillation counters or the time of flight was inconsistent with the measured energy or measured momentum; or if the trajectory did not pass through the hydrogen target and the incident photon beam; or if the incident photon energy, calculated with the assumption of Compton scattering or single-pion production, fell outside the kinematically possible range. Showers were rejected primarily if the pulse height in the shower counter was too low and, with certain additional restrictions, if the guard gaps indicated a charged particle origin of the shower.

With these criteria the rejections in the two arms were highly correlated, indicating they were not due to mismeasurement of a single parameter but involved a sample of events of a nature different from the accepted events. Further cuts were made after a kinematic fit of the complete event.

The interpretation of showers which appeared to contain particles in the initial guard gaps (veto gaps) caused some difficulty. We present an outline of the analysis of this problem as an illustration of the considerations leading to our values for the detection efficiency and errors. A significant fraction of showers starting in the first or second lead plates were apparently accompanied by one or more nearby sparks in the guard gaps. This number exceeded the number of background tracks. We conjecture that this phenomenon, also observed by other experimenters, is due to atomic x-rays and other soft radiation emitted in the backward direction. Figure 6 shows the pulse-height distribution in counter $S4$ for showers starting in the first and last useful lead plates and for all "particles" with sparks in the guard gaps. Manifestly, the latter represent a different type of event. When we applied all cuts to the recoil protons and required that the coordinates satisfy Compton or π^0 kinematics with high probability, the pulse-height

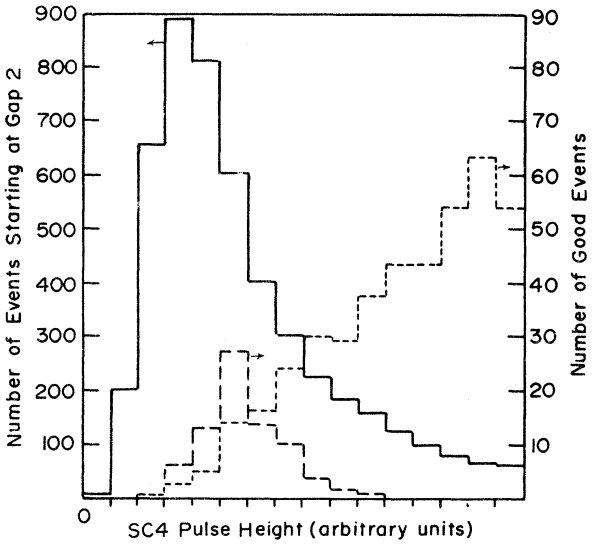

FIG. 6. Pulse-height spectra in lead glass counter unit *SC*4 in run *D*7. Solid line represents all showers starting in gap 2 of the shower chamber; short-dashed line represents showers from good events starting in gap 3; long-dashed line represents showers from good events starting in gap 19.

spectrum approached that for showers in gap 3. Pulse-height spectra of the shower counter showed similar behavior. The distribution of starting gaps for showers in "good" events followed the expected exponential attenuation in the shower chamber except for a deficiency of showers starting in the first or second lead plate. With the appropriate cuts, this deficiency was very nearly compensated by the remaining "particle"-initiated showers. Within rather poor statistics of the latter sample, its kinematic distribution agreed with that of the accepted events. We therefore decided to ignore the evidence of the guard gaps in these events.

The separation of the Compton events from the background—primarily single π^0 photoproduction—proceeded as follows. Each event was reconstructed from the proton energy and angle alone, assuming a Compton encounter. The event vertex was assumed to lie in the intersection of the proton trajectory and a vertical plane including the beam line. We then recorded the angular deviation, in the scattering angle and in the azimuth, of the line connecting this vertex with the observed shower origin from the predicted momentum vector of the scattered photon. Figure 7 shows a typical scatter plot of the events in one run. The elongated peak centered at zero deviation contains the Compton events. Figure 8 shows that the azimuthal spread $\Delta\phi$, which measures the deviation from coplanarity, is substantially smaller—typically a factor of three—than the spread in the kinematic angle $\Delta\theta$. The latter contains errors in energy determination and vertex position in addition to the errors of the position measurement. Very similar distributions are found if the event is reconstructed from both observed angles and the deviation of the observed photon energy or the missing mass is plotted on the abscissa.

Various procedures were used to interpolate the background under the peak, generally with concordant results. The dashed line in Fig. 8 was obtained by generating an uncorrelated sample of proton and shower data representative of the actual geometric situation. This was done by combining the shower data of each event with the proton data of the preceding event. The Jacobian of the π^0 decay does not vary significantly for the very small variation in ϕ. The deviation of the sample from randomness due to the small number of Compton events was found to be negligible. Thus the randomized distribution represents the variation of the background due to geometric factors alone and its shape was used to interpolate under the Compton peak. The distribution in θ (Fig. 8) is asymmetric, showing a tail corresponding to proton energies below that expected from a Compton event. This is typical of data obtained with the range chamber. Some of these events represent errors in range measurement of one or at most two gaps. Larger deviations correspond primarily to protons which are stopped by nuclear interactions before reaching the end of their range. We obtained good agreement between the observed number of such events and the known nuclear interaction cross sections. Many of these events were eliminated by the discrepancy between counter pulse height and range.

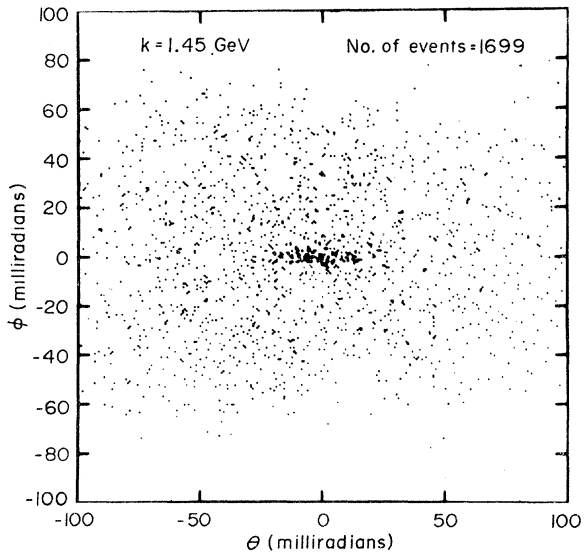

FIG. 7. Scatter plot for events in the shower chamber.

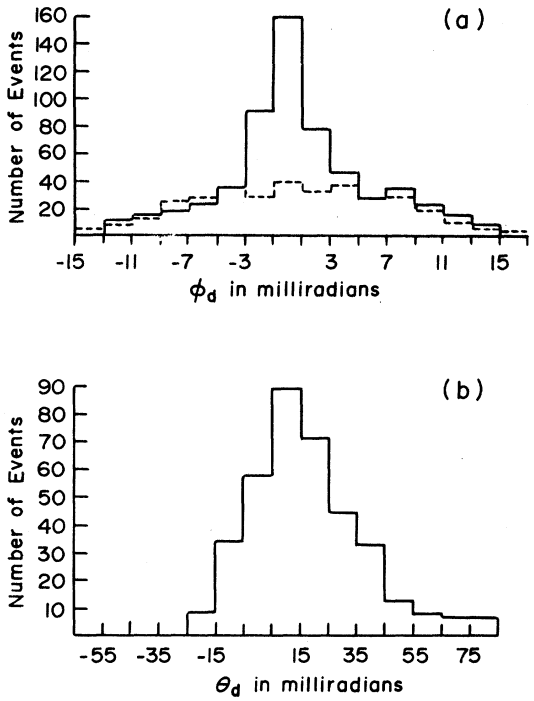

FIG. 8. Projections of the Compton peak from the scatter plots for run $D5$. (a) Azimuthal angle ϕ projection: ϕ_d = azimuthal deviation; solid line represents number of events at deviation ϕ_d for deviation θ_d between −25 and +35 milliradians; dashed line represents background. (b) Polar angle θ projection. θ_d = angular deviation in milliradians. Solid line represents number of events at polar deviation θ_d for azimuthal deviation θ_d between −3 and +3 milliradians.

We generally included these events with deviations not exceeding that due to a loss of two gaps and applied a correction to the data for the remaining losses.

Finally, we compared the observed number of events in the assumed π^0 background with the photoproduction cross sections and found agreement within the experimental uncertainties.

C. Cross-Section Calculation, Correction Factors, and Error Analysis

The cross section at a given t (the four-momentum transfer) and given s (the square of the center-of-mass energy) is given by

$$\frac{d\sigma}{dt}(s,t)=\frac{N}{(\Delta t)f},$$

where the various factors are defined as follows:

N: Observed number of Compton events occurring at the four-momentum transfer t in the interval Δt and averaged over the appropriate energy interval Δk. In series C, the interval Δt is given by $\Delta t=(dt/d\Omega_{\text{c.m.}})\Delta\Omega_{\text{c.m.}}$. In all other runs, t is directly given from the range-chamber information.

$$f=N_H\epsilon_\gamma\epsilon_s\epsilon_p\epsilon_{sc}\frac{(\Delta\phi)}{2\pi}\eta_0\eta_1 Q\frac{(\Delta k)}{k}\epsilon_{\text{mis}}.$$

N_H: Number of protons/cm^2 in the hydrogen target.

ϵ_γ: Conversion efficiency in the shower chamber.

ϵ_s: Shower detection efficiency. Accounts for losses by interactions in counter $S7$ and for scanning losses due to background tracks or anomalous shower development.

ϵ_p: Proton chamber efficiency. Accounts for scanning losses, mainly in $T1$ and in range chamber.

ϵ_{sc}: Counter dead-time correction.

$\Delta\phi$: Azimuthal acceptance, as discussed in Sec. B.

η_0: Correction for nuclear interactions in the proton counter telescope.

η_1: Correction for nuclear interactions in the range chamber, when applicable. Derivation of η_0 and η_1 is discussed in Ref. 9.

Q: Number of equivalent quanta for the given run. This involves calibration and correction for misscanned, otherwise lost events.

Δk: Incident γ-ray energy bin.

k: Mean energy in bin (k).

ϵ_{mis}: Miscellaneous efficiency factor containing corrections for bremsstrahlung shape function, for the efficiency of the proton range- or momentum-measuring system, and for losses from the proton geometrical cutoff near either end of the acceptance.

Values for these quantities are given in Table III.

The following are the major uncertainties in the above quantities, grouped into three categories:

(a) Statistical errors, primarily in N, the number of Compton events. These include the statistical uncertainity in the subtracted background. The statistical uncertainty of a typical point is ±15%.

(b) Systematic normalization errors which affect all points in a given run by the same factor. The following are typical examples:

N: ±3%,

Q: ±2% (but cf. discussion of run B in Sec. III A),

ϵ_γ: ±2%,

ϵ_{sc}: ±3%,

$\Delta\phi$: ±0.5%.

We estimate that the normalization error of an

TABLE III. Summary of correction factors and data. k_0 = end-point energy (in GeV) of the bremstrahlung spectrum; Q = number of equivalent quanta; N_H = number of target protons; ϵ_γ = efficiency of the γ chamber; ϵ_s = shower detection efficiency; ϵ_{sc} = scintillation counter efficiency; $\Delta\phi$ = azimuthal acceptance; $\eta_0\eta_1$ = nuclear interaction correction factor; Δk = incident γ-ray energy bin (GeV); $\bar{k}$ = mean energy in GeV; ϵ_{mis} = efficiency factor (see text);

$$f = QN_H\epsilon_\gamma\epsilon_s\epsilon_p\epsilon_{sc}\frac{\Delta\phi}{2\pi}\eta_0\eta_1\frac{\Delta k}{k}\epsilon_{mis}.$$

Δt = squared four-momentum transfer interval in $(\mathrm{GeV}/c)^2$; N = number events in bin; $\bar{t}$ = mean momentum transfer squared $(\mathrm{GeV}/c)^2$; $d\sigma/dt$ = differential cross section $[\mathrm{cm}^2/(\mathrm{GeV}/c)^2]$. The error bars include statistical and systematic uncertainties.

Run	k_0 (GeV)	$10^{-13}Q$	$10^{-23}N_H$	ϵ_γ	ϵ_s	ϵ_p	ϵ_{sc}	$10^3\frac{\Delta\phi}{2\pi}$	η_0	η_1	$\frac{\Delta k}{k}$	ϵ_{mis}	$10^{-34}f$	Δt	N	$\bar{k}$	$-\bar{t}$	$10^{30}\frac{d\sigma}{dt}$
*A*2	0.905	22.0	2.36	0.85	0.90	0.99	0.93	7.08	0.940	0.985	0.0526	0.906	1.142	0.0191	240	0.570	0.147	1.100 ± 0.106
										0.975	0.0500	0.902	1.070	0.0260	249	0.600	0.158	0.895 ± 0.085
										0.965	0.0476	0.091	1.007	0.0308	442	0.630	0.169	1.425 ± 0.102
$f_1 = QN_H\epsilon_\gamma\epsilon_s\epsilon_p\epsilon_{sc}\frac{\Delta\phi}{2\pi}\eta_0$										0.949	0.0454	0.902	0.946	0.0352	560	0.660	0.181	1.682 ± 0.107
$= 24.337\times10^{34}$										0.932	0.0434	0.902	0.889	0.0391	545	0.690	0.193	1.568 ± 0.101
										0.916	0.0417	0.899	0.836	0.0417	520	0.720	0.205	1.492 ± 0.098
										0.902	0.0400	0.891	0.782	0.0426	700	0.750	0.216	2.101 ± 0.101
										0.880	0.0385	0.880	0.726	0.0423	556	0.780	0.229	1.810 ± 0.115
										0.863	0.0370	0.863	0.671	0.0409	416	0.810	0.241	1.516 ± 0.111
										0.850	0.0357	0.835	0.617	0.0385	335	0.840	0.253	1.410 ± 0.116
*A*3	0.905	9.60	2.36	0.85	0.90	0.99	0.93	7.08	0.730	0.980	0.0531	0.906	0.389	0.0280	190	0.565	0.412	1.744 ± 0.190
										0.914	0.0504	0.902	0.343	0.0372	199	0.595	0.444	1.560 ± 0.166
										0.868	0.0480	0.901	0.310	0.0437	228	0.625	0.476	1.683 ± 0.167
$f_1 = 8.247\times10^{34}$										0.817	0.0458	0.902	0.278	0.0507	207	0.655	0.509	1.469 ± 0.153
										0.775	0.0438	0.902	0.252	0.0557	188	0.685	0.542	1.339 ± 0.147
										0.726	0.0420	0.900	0.226	0.0574	191	0.715	0.576	1.472 ± 0.160
										0.686	0.0403	0.892	0.203	0.0559	122	0.745	0.610	1.075 ± 0.146
										0.635	0.0387	0.882	0.179	0.0529	93	0.775	0.644	0.982 ± 0.153
										0.589	0.0370	0.866	0.157	0.0483	61	0.805	0.679	0.804 ± 0.154
B	1.500	4.37 [a]	3.03	0.85	0.90	0.99	0.93	6.91	0.91	0.91	0.059	0.87	0.274	0.0566	195	0.850	0.26	1.257 ± 0.135
										0.88	0.056	0.86	0.248	0.0808	182	0.900	0.28	0.908 ± 0.100
										0.85	0.053	0.84	0.222	0.1030	182	0.950	0.30	0.796 ± 0.089
$f_1 = 58.6210\times10^{33}$										0.79	0.050	0.84	0.195	0.1215	189	1.000	0.32	0.798 ± 0.087
$= QN_H\epsilon_\gamma\epsilon_s\epsilon_p\epsilon_{sc}\frac{\Delta\phi}{2\pi}\eta_0$										0.79	0.048	0.83	0.185	0.1346	135	1.050	0.34	0.542 ± 0.070
										0.76	0.046	0.83	0.170	0.1412	93	1.100	0.36	0.387 ± 0.060
										0.74	0.044	0.83	0.158	0.1390	78	1.150	0.38	0.355 ± 0.060
										0.70	0.042	0.83	0.143	0.1298	52	1.200	0.40	0.280 ± 0.058
										0.68	0.040	0.83	0.132	0.073	37	1.250	0.43	0.239 ± 0.060

TABLE III *(Continued)*

Run	k_0 (GeV)	$10^{-13}Q$	$10^{-23}N_H$	ϵ_γ	ϵ_s	ϵ_p	ϵ_{sc}	$10^3\frac{\Delta\phi}{2\pi}$	η_0	η_1	$\frac{\Delta k}{k}$	ϵ_{mis}	$10^{-34}f$	Δt	N	$\bar{k}$	$-\bar{t}$	$10^{30}\frac{d\sigma}{dt}$
$C1$	1.305	6.08	2.14	0.87	0.90	0.99	0.99	7.16	0.91	1.00	0.071	0.93	0.430	0.0424	237	0.700	0.242	1.300 ± 0.127
											0.067	0.91	0.396	0.0528	285	0.750	0.263	1.363 ± 0.121
$f_1 = 65.077 \times 10^{33}$											0.063	0.90	0.369	0.0608	250	0.800	0.283	1.114 ± 0.106
$= (QN_H\epsilon_\gamma\epsilon_s\epsilon_p\epsilon_{sc}\frac{\Delta\phi}{2\pi}\eta_0)$											0.059	0.89	0.342	0.0658	238	0.850	0.304	1.058 ± 0.103
											0.056	0.88	0.321	0.0709	207	0.900	0.325	0.910 ± 0.095
											0.053	0.88	0.304	0.0757	180	0.950	0.344	0.782 ± 0.087
											0.050	0.87	0.283	0.0806	146	1.000	0.364	0.640 ± 0.080
											0.048	0.87	0.272	0.0850	99	1.050	0.384	0.428 ± 0.065
											0.046	0.87	0.260	0.0873	102	1.100	0.402	0.449 ± 0.067
											0.044	0.85	0.243	0.0874	67	1.150	0.421	0.315 ± 0.058
											0.042	0.82	0.224	0.0836	55	1.200	0.439	0.294 ± 0.059
											0.040	0.76	0.198	0.0758	28	1.250	0.457	0.187 ± 0.053
$C2$	2.018	18.32	2.14	0.87	0.90	0.99	0.99	7.37	0.81	1.00	0.066	0.92	1.090	0.0948	310	1.138	0.463	0.300 ± 0.026
											0.062	0.90	1.002	0.1042	260	1.213	0.494	0.249 ± 0.023
$f_1 = 179.582 \times 10^{33}$											0.058	0.89	0.927	0.1124	150	1.288	0.524	0.144 ± 0.018
											0.055	0.88	0.869	0.1193	122	1.363	0.553	0.118 ± 0.016
											0.052	0.88	0.821	0.1263	130	1.438	0.582	0.125 ± 0.016
											0.050	0.87	0.781	0.1329	90	1.513	0.610	0.0867 ± 0.014
											0.047	0.87	0.734	0.1381	67	1.588	0.636	0.0661 ± 0.012
											0.045	0.87	0.703	0.1390	60	1.663	0.663	0.0614 ± 0.012
											0.043	0.86	0.664	0.1308	45	1.738	0.687	0.0518 ± 0.012
											0.041	0.85	0.626	0.1152	33	1.813	0.713	0.0458 ± 0.012
											0.040	0.81	0.582	0.0943	40	1.888	0.736	0.0729 ± 0.017
$C3$	2.700	13.68	2.14	0.87	0.90	0.99	0.99	7.67	0.81	1.00	0.133	0.92	1.708	0.0821	120	1.500	0.692	0.0856 ± 0.012
											0.118	0.90	1.483	0.1543	105	1.700	0.773	0.0459 ± 0.0067
$f_1 = 139.601 \times 10^{33}$											0.105	0.88	1.290	0.1785	90	1.900	0.850	0.0391 ± 0.0062
											0.095	0.87	1.154	0.9165	47	2.100	0.920	0.0207 ± 0.0045
											0.087	0.87	1.057	0.2149	42	2.300	0.986	0.0185 ± 0.0043
											0.080	0.82	0.916	0.2315	16	2.500	1.048	0.0075 ± 0.0028

TABLE III *(Continued)*

Run	$10^{-13}Q$	$10^{-23}N_H$	ϵ_γ	ϵ_s	ϵ_p	ϵ_{sc}	$10^3\frac{\Delta\phi}{2\pi}$	η_0	η_1	$\frac{\Delta k}{k}$	ϵ_{mis}	$10^{-34}f$	Δt	N	$\bar{k}$	$-\bar{t}$	$10^3\frac{d\sigma}{dt}$
$D1$	4.42	2.27	0.82	0.87	0.97	0.93	11.14	0.97	0.98	0.20	0.87	0.119	0.032	206	1.45	0.140	0.50 ± 0.05
									0.95	0.20	0.89	0.118	0.039	253	1.60	0.178	0.53 ± 0.05
$f_1 = 69.77\times10^{33}$									0.90	0.20	0.89	0.112	0.034	146	1.80	0.213	0.35 ± 0.04
									0.87	0.20	0.90	0.109	0.039	151	1.98	0.248	0.33 ± 0.04
									0.85	0.20	0.81	0.0961	0.043	136	2.10	0.290	0.28 ± 0.05
$D2$	6.20	2.27	0.82	0.87	0.97	0.90	11.46	0.95	0.98	0.25	0.87	0.203	0.037	303	2.40	0.162	0.40 ± 0.03
									0.94	0.25	0.89	0.200	0.044	251	2.70	0.201	0.28 ± 0.03
$f_1 = 95.43\times10^{33}$									0.90	0.17	0.91	0.133	0.032	116	3.00	0.238	0.28 ± 0.03
									0.87	0.17	0.91	0.128	0.042	103	3.10	0.275	0.19 ± 0.03
$D3$	3.48	2.27	0.82	0.87	0.97	0.90	11.55	0.95	0.98	0.25	0.81	0.107	0.037	138	2.40	0.162	0.35 ± 0.06
									0.94	0.25	0.81	0.114	0.044	150	2.70	0.201	0.30 ± 0.03
$f_1 = 53.98\times10^{33}$									0.89	0.25	0.90	0.108	0.039	94	3.00	0.243	0.22 ± 0.03
									0.86	0.25	0.89	0.103	0.053	110	3.40	0.290	0.20 ± 0.03
									0.80	0.25	0.89	0.0961	0.048	94	3.75	0.340	0.21 ± 0.04
$D4$	2.51	2.27	0.82	0.87	0.97	0.90	11.55	0.95	0.98	0.21	0.92	0.0737	0.037	154	2.00	0.162	0.48 ± 0.05
									0.94	0.21	0.91	0.0699	0.044	144	2.20	0.201	0.42 ± 0.04
$f_1 = 38.94\times10^{33}$									0.89	0.21	0.90	0.0655	0.039	105	2.45	0.243	0.37 ± 0.05
									0.86	0.21	0.89	0.0626	0.053	72	2.65	0.290	0.18 ± 0.03
									0.80	0.21	0.89	0.0582	0.048	51	2.85	0.340	0.16 ± 0.03
$D5$	4.60	2.27	0.82	0.87	0.97	0.90	11.30	0.95	0.98	0.28	0.88	0.169	0.037	228	3.40	0.162	0.36 ± 0.03
									0.94	0.28	0.89	0.164	0.044	191	3.75	0.201	0.26 ± 0.03
$f_1 = 69.81\times10^{33}$									0.89	0.28	0.89	0.155	0.039	118	4.15	0.243	0.19 ± 0.03
									0.86	0.28	0.77	0.129	0.053	121	4.60	0.290	0.18 ± 0.04
$D6$	4.55	2.27	0.82	0.87	0.97	0.90	11.30	0.95	0.98	0.23	0.88	0.137	0.037	180	2.70	0.162	0.35 ± 0.03
									0.94	0.23	0.89	0.133	0.044	191	3.10	0.201	0.32 ± 0.03
$f_1 = 69.05\times10^{33}$									0.89	0.23	0.89	0.126	0.039	124	3.40	0.243	0.24 ± 0.03
									0.86	0.23	0.77	0.105	0.053	114	3.70	0.290	0.20 ± 0.04
$D7$	1.57	2.27	0.82	0.80	0.97	0.90	11.70	0.84	0.99	0.20	0.87	0.0346	0.024	170	3.10	0.280	0.20 ± 0.02
									0.97	0.20	0.89	0.0346	0.031	186	3.25	0.300	0.18 ± 0.02
$f_1 = 20.06\times10^{34}$									0.91	0.20	0.89	0.0325	0.031	143	3.43	0.340	0.14 ± 0.02
									0.87	0.20	0.89	0.0311	0.043	182	3.62	0.370	0.14 ± 0.01
									0.82	0.20	0.91	0.0299	0.043	135	3.82	0.410	0.11 ± 0.015

[a] Corrected for normalization factor of 1.4 (see text).

individual run is about ±7% with a common overall scale uncertainty of about ±10%.

(c) Other systematic errors, affecting individual cross-section values.

(i) The incident photon spectrum is of the form

$$N(k)\Delta k = QS(k)\Delta k/k,$$

$S(k) \simeq 0.9$ within a few percent, in all cases. Calculated values of $S(k)$ are included in the factor ϵ_{mis} and are believed to be reliable to ±1% in most cases.

(ii) Nuclear interactions in the range-chamber plates were assumed to reduce the number of protons by a factor $\eta_1 = \exp(-\alpha R)$, where $\alpha = 8.9 \times 10^{-3}$ cm^2/g Al and R is the residual range of the protons when entering the range chamber. The uncertainty in the factor $(1-\eta_0\eta_1)$ is estimated to be ±3%.

(iii) The main uncertainty in the scanning efficiency for protons arose in occasional failure of SPASS to follow a track to the end of its range. There could be a correlation of this failure with range and angle. We estimate the error in ϵ to be about ±3%. (About 10% of the valid shower pictures could not be measured because of background tracks. We estimate the uncertainty in ϵ to be about ±3%.)

(iv) The uncertainty in background subtraction is discussed separately, in Sec. IV B.

V. RESULTS

Our results are summarized in Table III. Each entry in the table includes data for a kinematic interval, typically $\Delta k/k = 0.2$, $\Delta t = 0.04$ (GeV/c)^2. The indicated uncertainty is the expected standard deviation, including systematic errors, of the individual points. It does not include the common normalization uncertainty.

A. Large-Angle Measurements

The low-energy data in series B and C were collected at fairly constant center-of-mass angles, 65°, 90°, and 115°, respectively, so that any resonant structure in the differential cross section would be evident. These are plotted in Fig. 9. We have also included data in the same energy range from Refs. 9 and 10.

1. General Features

It is evident that the second resonance $D_{13}(1520)$ stands out quite clearly. In contrast the third resonance $F_{15}(1688)$ is not pronounced. It appears more like a shoulder at approximately 1-GeV incident kinetic energy. The differential cross section thereafter continues to fail quite steeply. The very precise total cross-section measurements of Ref. 17 in this energy range also show the same features—except that the structure at 1 GeV is slightly more pronounced.

We also show, for reference and comparison, the forward Compton cross section *calculated* from the total cross section measurements of Ref. 17, and the use of the optical theorem for the imaginary part of the forward amplitude, and the dispersion relation of Gell-Mann, Goldberger, and Thirring[1] for the real part.

$$\mathrm{Re}f(k) = -\frac{e^2}{M} + \frac{k^2}{2\pi^2}\mathcal{P}\int_{k_0}^{\infty}\frac{\sigma_T(k')}{k'^2-k^2}\,dk',$$

$$\left.\frac{d\sigma}{dt}\right|_{t=0} = \frac{\sigma_T^{\,2}}{16\pi}\left[1+\left(\frac{\mathrm{Re}f}{\mathrm{Im}f}\right)^2\right] + \frac{\pi}{k^2}|f_2(k)|^2.$$

The high-energy total cross section was parametrized[17] by $\sigma_T \to 91.0 + 71.4(k)^{-1/2}$ μb, and f_2, the high-energy spin-dependent amplitude, was set to zero. See also Ref. 18.

2. Comparison with Vector-Dominance Model

According to VDM, Compton scattering and vector-meson photoproduction are related[4] by

$$\frac{d\sigma(\gamma p\to\gamma p)}{dt} = \left\{\sum_V\left[\frac{\pi\alpha}{\gamma_V^{\,2}}\frac{d\sigma^T}{dt}(\gamma p\to Vp)\right]^{1/2}\right\}^2,$$

where $d\sigma^T/dt$ is the cross section for transversely polarized vector mesons $V(\rho^0, \omega, \phi)$ and γ_V is the photon–vector-meson coupling constant. This relation is an *upper* limit, corresponding to maximum constructive interference between the vector-meson production amplitudes. The coupling constants γ_V are those obtained in the storage-ring experiments.[19] The photoproduction data are from the DESY Bubble Chamber group.[7] Inadequate statistics forced that group to bin their data in very large incident energy intervals ($1.4 < k < 1.8$ GeV and $1.8 < k < 2.5$ GeV) and in very large angular interval $0.25 < \cos\theta < 0.5$. Hence, until better photoproduction data become available, it is not possible to make a precise statement about agreement between this experiment and VDM. Columns 3 and 4 of Table IV show, however, that VDM underestimates the Compton cross section by a factor of almost 2 to 3. We remark that question of how one extracts the ρ^0 photoproduction from the observed two-pion photoproduction is important for the above comparison since the various alternatives suggested[6] can make an almost 50% difference. While more accurate ρ^0 photoproduction data and more reliable methods of analyzing them are necessary to make the disagreement quantitative, it seems to us that the role of the vector-meson masses in

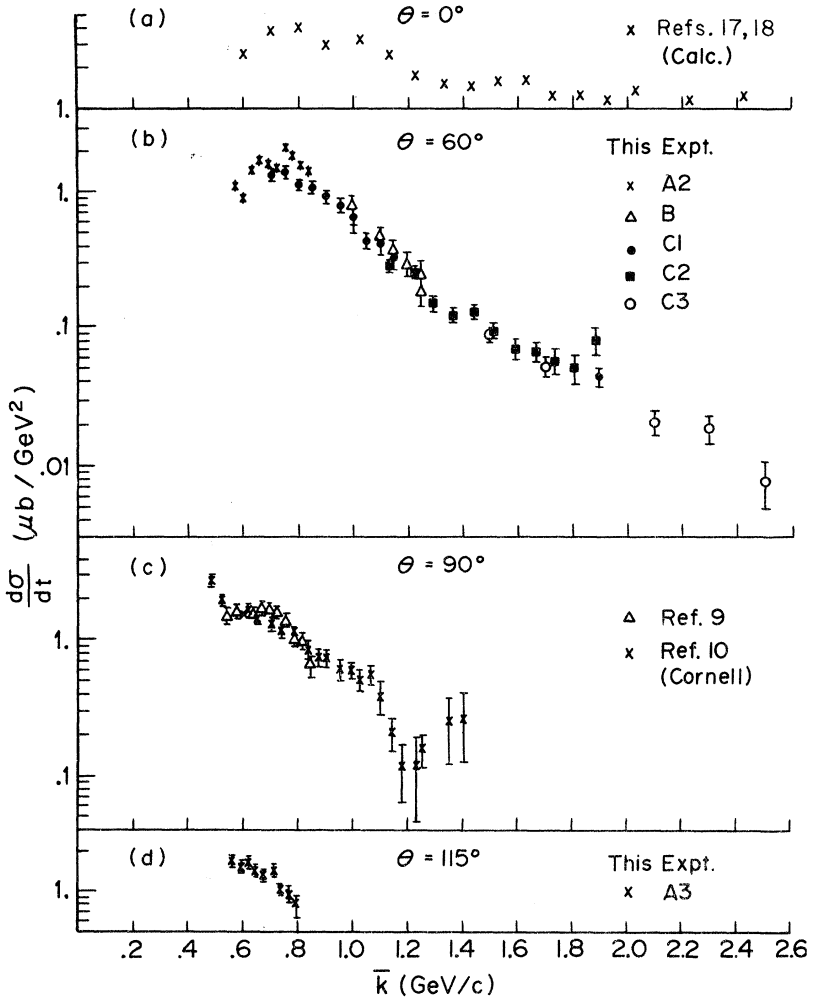

FIG. 9. (a) Zero-degree cross section calculated using dispersion relations (see text); (b)-(d) large-angle cross section $d\sigma/dt$ as a function of incident energy. θ^* = scattering angle in c.m. frame.

VDM comparisons must be reexamined. We shall reinforce this conclusion in the next section, where possible ρ' contribution is discussed.

B. Small-Angle Measurements

The data points are shown in Fig. 10 and are averages, over the energy intervals indicated, of the entries in Table III.

1. General Features

A least-squares fit to the data, for $k = 3.2 \pm 0.6$ GeV, of the form $d\sigma/dt = A \exp(Bt)$ yields

$$A = 735 \pm 93 \text{ nb/(GeV/}c)^2,$$

$$B = 4.6 \pm 0.4 \text{ (GeV/}c)^{-2}.$$

A represents the forward cross section. Following the procedure in Sec. VI A, we calculated the expected[17] forward cross section to be (990 ± 100) μb/GeV/$c)^2$ at $k = 3.2$ GeV. This is consistent with the value of A we obtain above.

Since the constant A is determined so poorly in the Compton experiment, we found it advisable to obtain the best value of the slope B by making a one-parameter least-squares fit to the data of the

TABLE IV. Comparison of large-angle experimental results with the vector-dominance model (VDM) predictions.

$\bar{k}$ (GeV)	$\cos\theta_C$	$\frac{d\sigma}{dt}$ [cm²/(GeV/c)²]	
		Experiment	VDM prediction
1.6 ± 0.2	0.4 ± 0.1	$(65 \pm 13) \times 10^{-33}$	$(27 \pm 12) \times 10^{-33}$
2.2 ± 0.3	0.4 ± 0.1	$(20 \pm 4) \times 10^{-33}$	$(7 \pm 5) \times 10^{-33}$

form $d\sigma/dt = (990 \pm 100)\exp(Bt)$. The value of the slope we obtain is $B = 5.0 \pm 0.3$ $(\mathrm{GeV}/c)^{-2}$.

We followed the same procedure for the small-angle data for $k = 2.0 \pm 0.5$ GeV. The one-parameter least-square fit used is

$$\frac{d\sigma}{dt} = (1250 \pm 125)\exp(Bt)$$

where the value of the expected forward cross section was calculated as above.[17] The best value of B we obtain is

$$5.3 \pm 0.5\ (\mathrm{GeV}/c)^{-2}.$$

Figure 10 also shows the large-angle data for the same energy range from run C. These data can be fitted with an exponential form having a slope parameter $B = 4.5 \pm 0.4$ $(\mathrm{GeV}/c)^{-2}$. It is remarkable that B is so close to the diffraction slope B, and this calls for further theoretical analysis.

The data for $k > 4$ GeV fall significantly below the values for the lower energies at the same momentum transfers, and are consistent with the values obtained by the DESY Group.[13]

Recent data reported by the Daresbury group[20] in the energy range 0.65 to 1.35 GeV are in agreement with our results.

2. *Comparison with Vector-Dominance Model*

It is of interest to compare the diffraction slope in Compton scattering with corresponding values for vector-meson production. As Table V shows, results on ρ^0 photoproduction indicate a slope

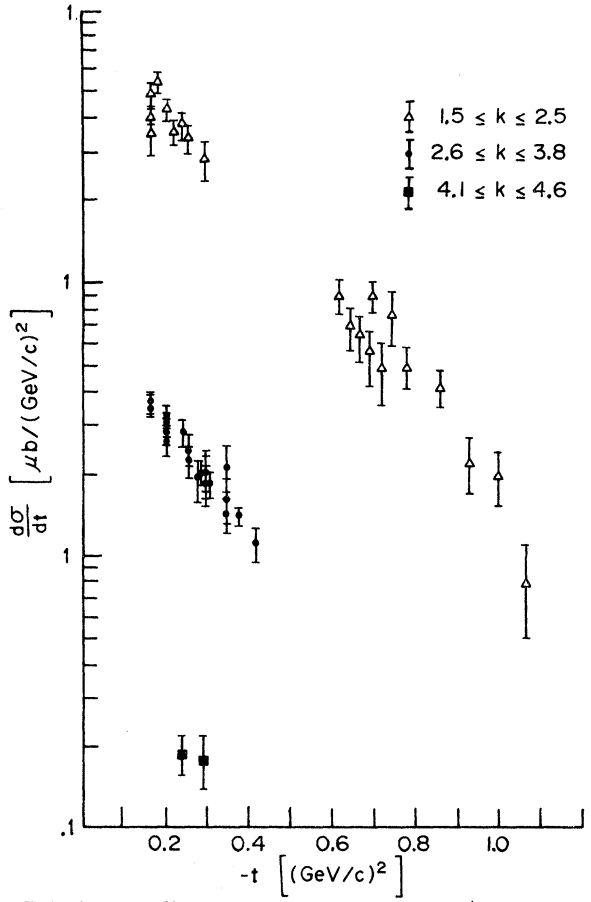

FIG. 10. Small-angle results plotted as $d\sigma/dt$ vs t. See Table VI for parametrization of the data.

TABLE V. Compilation of vector-meson photoproduction results used in calculating VDM predictions in Table VI.

Reaction	k_γ (GeV)	t range (GeV^2)	A (μb GeV^{-2})	b (GeV^{-2})	Model	Ref.
$\gamma+p\to\rho^\circ+p$	1.5–2.5	0.05–0.5	135 ± 15	5.6 ± 0.5	Ross-Stodolsky	ABBHHM[7]
	2.0–2.5	0.06–0.4	134 ± 20	6.4 ± 0.8	Söding	SWT[a]
	2.5–3.0	0.06–0.4	177 ± 26	8.8 ± 1.1	Söding	SWT[a]
	2.8	0.02–0.4	138 ± 8	6.6 ± 0.3	Söding	SBT[6]
	3.0		156 ± 12		Ross-Stodolsky	Desy-MIT
	2.5–3.5	0.05–0.5	147 ± 13	6.9 ± 0.4	Ross-Stodolsky	ABBHHM[7]
	3.0–3.7	0.06–0.4	124 ± 20	7.5 ± 1.2	Söding	SWT[a]
	3.7–4.7	0.06–0.4	101 ± 12	6.5 ± 0.5	Söding	SWT[a]
	4.7	0.02–0.4	94 ± 6	5.9 ± 0.3	Söding	SBT[6]
$\gamma+p\to\omega^\circ+p$	1.8–2.5		37 ± 8.1	5.4 ± 1.0		ABBHHM[7]
	2.8		34 ± 4	6.2 ± 0.7		SBT[6]
	2.8		13 ± 4	5.5 ± 1.6	Natural parity exchange	
	4.7		25 ± 3	8.0 ± 0.8		SBT[6]
			15 ± 4	7.5 ± 1.5	Natural parity exchange	SBT[6]
$\gamma+p\to\phi^\circ+p$	1.6–2.5		1.1 ± 0.7	2.7 ± 1.1		ABBHHM[7]
	2.5–5.8		1.6 ± 0.6	3.5 ± 0.9		ABBHHM[7]

[a] SLAC–Weizmann–Tel-Aviv Collaboration, in *Proceedings of the International Symposium on Electron and Photon Interactions at High Energies*, edited by N. B. Mistry (Ref. 5).

TABLE VI. Parametrization of the Compton small-angle results in the form $d\sigma/dt = Ae^{bt}$ and comparison with predictions of the VDM model ($\gamma_\rho{}^2/4\pi = 0.64 \pm 0.06$; $\gamma_\omega{}^2/4\pi = 4.6 \pm 0.5$; $\gamma_\phi{}^2/4\pi = 2.9 \pm 0.2$).

k (GeV)	t range $(\mathrm{GeV}/c)^2$	Experiment A	b	Ref.	VDM prediction A	
1.5–2.5	0.1–0.25	1.25 ± 0.13	5.3 ± 0.5	Present exp.	0.60	
2.2–2.7	0.1–0.4	1.26 ± 0.13	5.2 ± 0.5	Ref. 13	0.50	
2.7–3.2	0.1–0.4	1.14 ± 0.11	5.7 ± 0.4	Ref. 13	0.74	SWT[a]
					0.45	SBT[6]
2.6–3.8	0.15–0.4	0.99 ± 0.10	5.0 ± 0.3	Present exp.	0.48	
3.2–3.7	0.1–0.4	1.24 ± 0.11	6.2 ± 0.4	Ref. 13	0.50	
3.7–4.2	0.1–0.4	1.02 ± 0.14	5.3 ± 0.5	Ref. 13	0.40	

[a] SLAC–Weizmann–Tel-Aviv Collaboration, in *Proceedings of the International Symposium on Electron and Photon Interactions at High Energies*, edited by N. B. Mistry (Ref. 5).

ranging from 5.6 to 8.8 $(\mathrm{GeV}/c)^{-2}$. It is seen that even experiments employing substantially the same model to treat the nonresonant background report conflicting values. The slope for ω photoproduction through natural parity exchange seems to be approximately 6 $(\mathrm{GeV}/c)^{-2}$ in this energy range. We are forced to conclude that until the ρ^0 photoproduction data become more definitive the comparison of diffraction slopes is not meaningful.

Comparison of the extrapolated cross section at $t = 0$ also shows a contradiction with naive VDM. Table VI summarizes these results and also gives a comparison of our experimental data with those of Buschhorn *et al.*[13] It emphasizes once again the consistency of the experimental data on Compton scattering from the various laboratories.

Our conclusions are not altered by the recent reports about the $J^P = 1^-$ enhancement ρ' in the four-pion mass spectrum in e^+-e^- annihilation[21] and photoproduction experiments[22,23] at approximately 1.6-GeV/c^2 mass. While there is good evidence for the bump, the values of the coupling constant, $\gamma_{\rho'}{}^2/4\pi$, and the ρ' photoproduction cross section are still uncertain. The upper limit for the ratio

$$R = \left(\frac{\gamma_\rho{}^2}{\gamma_{\rho'}{}^2}\right) \frac{d\sigma}{dt}(\gamma \to \rho') \Big/ \frac{d\sigma}{dt}(\gamma \to \rho)$$

is of the order of 0.12. R has to be of the order of 0.5 before the discrepancies reported in Tables V and VI can be explained.

The series of experiments reported here must be viewed in the context of other Compton-effect and photoproduction experiments at higher energies[5] where deviations from the predictions of the vector-dominance model have been also been observed.

ACKNOWLEDGMENTS

It is a pleasure to thank the Directors and Staff of the Cornell Synchrotron and the Cambridge Electron Accelerator for their cooperation in the installation of the experiment and in providing optimum beam conditions. One of us (PMP) would like to thank G. F. Hartner for computational assistance.

*Work supported through funds provided by the U. S. Atomic Energy Commission under Contract No. AT (11-1)-3069.

†Present address: International Business Machines, New Delhi 1, India.
‡Present address: American Science and Engineering, Cambridge, Mass. 02139.
§Present address: Department of Physics, University of Massachusetts, Amherst, Mass. 01002.
‖Present address: Department of Physics and Wilson Laboratory, Cornell University, Ithaca, N. Y. 14850.
**Present address: Istituto di Fisica dell'Università di Roma and Sezione di Roma dell'Istituto Nazionale di Fisica Nucleare, Roma, Italy.
††Present address: Department of Physics, McGill University, Montreal, Quebec, Canada.
‡‡Present address: Department of Physics, Northeastern University, Boston, Mass. 02115.
§§Present address: National Accelerator Laboratory, Batavia, Illinois 60510.
‖‖Present address: Department of Biology, Massachusetts Institute of Technology, Cambridge, Mass. 02139.

[1] M. Gell-Mann, M. Goldberger, and W. Thirring, Phys. Rev. 95, 1612 (1954).
[2] P. M. Patel, AEC Report No. AEC-TJD 24667, 1967 (unpublished), p. 567; D. V. Skobel'tsyn, Proc. Lebedev Physics Institute, Vol. 141, 1969 (Translated into English by Consultants Bureau, New York, N. Y.).

[3]S. Minami, Nuovo Cimento 21, 401 (1961).
[4]A. Dar, V. F. Weisskopf, C. A. Levinson, and H. J. Lipkin, Phys. Rev. Lett. 20, 1261 (1968).
[5]G. Wolf, in *Proceedings of the International Symposium on Electron and Photon Interactions at High Energies,* edited by N. B. Mistry (Laboratory of Nuclear Studies, Cornell University, Ithaca, N. Y., 1972), p. 189.
[6]SLAC-Berkeley-Tufts Collaboration, Phys. Rev. Lett. 24, 955 (1970).
[7]Aachen-Berlin-Bonn-Hamburg-Heidelberg-München Collaboration, Phys. Rev. 175, 1669 (1968).
[8]M. Deutsch, E. Loh, P. M. Patel, and I. Afnan, Lab. Nuc. Sc. M.I.T. Prog. Report No. 82, 1963 (unpublished); M. Deutsch, E. Loh, P. M. Patel, and R. F. Stiening, Bull. Amer. Phys. Soc. 9, 374 (1964); M. Deutsch, J. Cleetus, E. Loh, and P. M. Patel, *ibid.* 10, 446 (1965); M. Deutsch, E. Loh, G. Marini, P. M. Patel, and K. Tsipis, in *Proceedings of the Third International Symposium on Electron and Photon Interactions at High Energies, Stanford Linear Accelerator Center, Stanford, California, 1967* (Clearing House of Federal Scientific and Technical Information, Washington, D. C., 1968); M. Deutsch and D. F. Jacobs, in *High Energy Physics,* proceedings of the Fifteenth International Conference on High Energy Physics, Kiev, 1970, edited by V. Shelest (Naukova Dumka, Kiev, U.S.S.R., 1972); also Bull. Amer. Phys. Soc. 15, 608 (1970).
[9]R. F. Stiening, E. Loh, and M. Deutsch, Phys. Rev. Lett. 10, 536 (1963).
[10]D. R. Rust, E. Eisenhandler, P. J. Mostek, A. Silverman, C. K. Sinclair, and R. M. Talman, Phys. Rev. Lett. 15, 938 (1965).
[11]B. Kenton, thesis, Caltech, 1968 (unpublished).
[12]R. L. Anderson, D. Gustavson, J. Johnson, I. Overman, D. Ritson, B. H. Wiik, R. Talman, J. K. Walker, and D. Worcester, Phys. Rev. Lett. 25, 1218 (1970).
[13]G. Buschhorn, L. Criegee, K. Duval, G. Franke, C. Geweniger, P. Heide, R. Kotthaus, G. Poelz, U. Timm, K. Wegener, H. Werner, M. Wong, and W. Zimmerman, Phys. Lett. 33B, 241 (1970); G. Buschhorn, L. Criegee, G. Franke, P. Heide, R. Kotthaus, G. Poelz, U. Timm, G. Vogel, K. Wegener, H. Werner, and W. Zimmerman, Phys. Lett. 37B, 207 (1971); 37B, 211 (1971).
[14]A. M. Boyarski, D. H. Coward, S. Ecklund, B. Richter, D. Sherden, R. Siemann, and C. Sinclair, Phys. Rev. Lett. 26, 1600 (1971).
[15]H. Rudloe, M. Deutsch, T. Marrill, Commun. ACM (Assoc. Comput. Mach.) 6, 332 (1963); M. Deutsch, IEEE Trans. Nucl. Sci. *NS-12,* 69 (1965).
[16]D. Cutts, R. Stiening, C. Wiegand, and M. Deutsch, Phys. Rev. 184, 1380 (1969).
[17]T. A. Armstrong, W. R. Hogg, G. M. Lewis, A. W. Robertson, G. R. Brookes, A. S. Clough, J. H. Freeland, W. Galbraith, A. F. King, W. R. Rawlinson, N. R. S. Tait, J. C. Thomson and D. W. L. Tolfree, Daresbury Nuclear Physics Lab. Report No. P88 1971 (unpublished).
[18]M. Damashek and F. J. Gilman, Phys. Rev. D 1, 1319 (1970).
[19]J. LeFrançois, in *Proceedings of the International Symposium on Electron and Photon Interactions at High Energies,* edited by N. B. Mistry (Ref. 5).
[20]J. S. Barton, P. S. L. Booth, L. J. Carroll, J. R. Halt, A. P. Hufton, J. N. Jackson, G. Moscati, J. H. Norem, and J. R. Wormald, Phys. Lett. 42B, 297 (1972).
[21]G. Barbarino, M. Grilli, E. Iarocci, P. Spillantini, V. Valente, R. Visentin, F. Ceradini, M. Conversi, L. Paoluzi, R. Santonico, M. Nigro, L. Trasatti, and G. T. Zorn, Nuovo Cimento Lett. 3, 689 (1972).
[22]F. F. Liu, M. Davier, I. Derado, D. C. Fries, R. Z. Mozley, A. C. Odian, J. Park, W. P. Swanson, F. Villa, and D. Yount, Nucl. Phys. B47, 1 (1972).
[23]G. Smadija, H. H. Bingham, W. B. Fretter, W. J. Podolsky, M. S. Rabin, A. H. Rosenfeld, G. P. Post, J. Ballam, G. B. Chadwick, Y. Eisenberg, E. Kogan, K. C. Moddeit, P. Seyboth, I. O. Skillicorn, H. Spitzer, and G. Wolf, in *Experimental Meson Spectroscopy—1972,* proceedings of the Third International Conference, Philadelphia, 1972, edited by Kwan-Wu Lai and Arthur H. Rosenfeld (A.I.P., New York, 1972).